



Power Electronic Systems
Laboratory

© 2020 IEEE

IEEE Transactions on Industrial Electronics, Vol. 68, No. 1, pp. 744-755, January 2021

Dynamic Electromechanical Model and Position Controller Design of a New High-Precision Self-Bearing Linear Actuator

S. Miric,
R. Giuffrida,
D. Bortis,
J.W. Kolar

Personal use of this material is permitted. Permission from IEEE must be obtained for all other uses, in any current or future media, including reprinting/republishing this material for advertising or promotional purposes, creating new collective works, for resale or redistribution to servers or lists, or reuse of any copyrighted component of this work in other works.



Eidgenössische Technische Hochschule Zürich
Swiss Federal Institute of Technology Zurich

Dynamic Electromechanical Model and Position Controller Design of a New High-Precision Self-Bearing Linear Actuator

Spasoje Mirić, *Student Member, IEEE*, Rosario Giuffrida, *Student Member, IEEE*, Dominik Bortis, *Member, IEEE*, and Johann W. Kolar, *Fellow, IEEE*

Abstract—Direct drive tubular linear actuators (TLAs) may be used in various applications that require fast movements and high-precision positioning, e.g. pick-and-place robots. This paper presents the analysis, dynamic electromechanical model derivation, controller design and system operation of a TLA with integrated magnetic bearings (MBs). Furthermore, the actuator operation is verified with extensive measurements on the prototype, which include axial position step response, standard deviation of the steady-state positions and mover tilting control. Compared to any conventional TLA, which may perform only linear motion, the mover tilting control is possible due to integrated MBs. This gives the new actuator a great advantage in high-precision positioning systems, since any thermal expansions of the parallel kinematics may be compensated.

Index Terms—Active Magnetic Bearings, Linear Motor, Magnetic Levitation, MIMO System, Self-bearing, Tubular Linear Actuator.

I. INTRODUCTION

IN applications that require repetitive linear motion, the usage of direct drive tubular linear actuators (TLAs) is beneficial compared to systems where gearboxes are used to generate linear motion from a rotary actuator [1], [2]. Direct drive TLAs achieve higher dynamics, are more precise, and feature less moving parts that are subject to wear. They are gaining attention in numerous applications, such as actuators for pick-and-place robots in the semiconductor or electronics manufacturing industries [3]–[5], active and semi-active suspension systems [6], compressors [7], tubular linear generators [8], steering systems [9] or rehabilitation robots [10]. Nevertheless, in precision sensitive applications, accuracy and fast motion control of the direct-drive actuators may be affected by friction of the bearings and/or thermal expansions (e.g. in robotic arms that move the actuator). As a step forward in the actuator area, a contact-less TLA was proposed in [11] that features integrated active magnetic bearings (AMBs). With such an actuator, friction is removed and any thermal expansion may be compensated by adjusting the radial position of the AMB [12]. In addition, the stiffness of the bearings

This work was supported by ETH Research Grant ETH-13 16-2. Moreover, the authors acknowledge the support of CADFEM (Suisse) AG concerning the ANSYS software. Warm thanks also go to Fabian Dietschi for implementing the initial control system firmware.

All authors are with the Power Electronic Systems Laboratory, Swiss Federal Institute of Technology (ETH) Zurich, 8092 Zurich, Switzerland (S. Mirić is the corresponding author, e-mail: miric@lem.ee.ethz.ch).

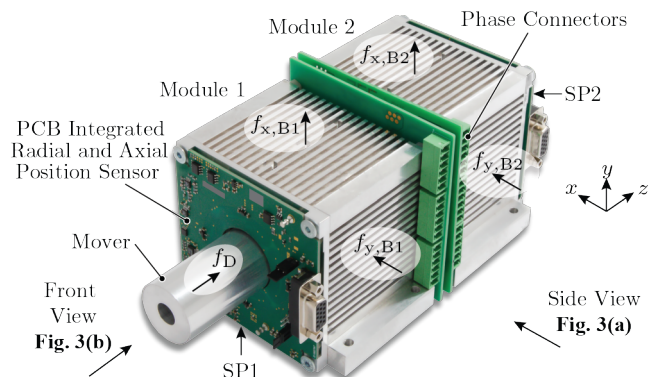


Fig. 1: MALTA prototype consisting of two stator modules that contain the phase coils, a mover comprising permanent magnets, and two PCB-integrated position sensors (SP1 and SP2). The shaft diameter is 27 mm, while the actuator active length is 170 mm. The machine design procedure is described in detail in [11]. The MALTA modules (stator) can act onto the mover with the bearing (radial) forces $f_{x,B\{1,2\}}$ and $f_{y,B\{1,2\}}$ in x - and y -direction and with the drive (linear) force f_D in z -direction.

and the tilting of the mover may be actively controlled. The proposed actuator is called MALTA (Magnetically Levitated Tubular Actuator) and its hardware prototype is shown in **Fig. 1**. In addition to the linear motion and magnetic bearings, to obtain the rotation, the MALTA concept may be extended and adapted, e.g. by adding a rotary machine, cf. [13].

In [11], only the magnetic design and the manufacturing aspects of the MALTA were analyzed, while this paper now focuses onto the control system design. In industry, PID position controllers are widely adopted for conventional TLAs [14], which are in general well suited for single-input single-output control schemes. However, they are unsuitable for the considered MALTA system, as for the positioning of the magnetically levitated mover five degrees of freedom have to be controlled simultaneously (instead of just one), resulting in a multiple-input multiple-output (MIMO) control problem. The controlled five degrees of freedom refer to: *forward-back*, *right-left*, *up-down*, *pitch* and *yaw*, whereas the sixth degree of freedom of the MALTA's mover, *rotation*, is not controllable. Therefore, a dynamic model of the mechanical subsystem of the MALTA is developed, which is used to design an appropriate MIMO feedback controller structure, which is assisted by additional feedforward compensation components.

The contributions of this manuscript are divided into the following sections: In **Sec. II**, a system model of the MALTA that considers the most relevant mechanical and electrical dynamics is derived. In **Sec. III**, the mechanical system model

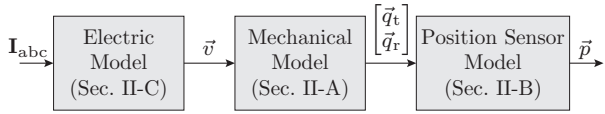


Fig. 2: Overview of the MALTA system models: the electric, mechanical and position sensor model.

is analyzed by linearizing the system and deriving the unstable poles. The position controller structure is proposed in **Sec. IV**, where also the current controller design is outlined. The system operation and measurement results, which verify the actuator operation and the mover tilting control, are shown in **Sec. VI**. Finally, **Sec. VII** concludes the paper.

II. MALTA SYSTEM MODEL

The MALTA system model consists of three parts: the electric model, the mechanical model and the position sensor model, as shown in **Fig. 2**.

The electric model elaborates the bearing and the drive force generation from the phase currents I_{abc} . For the derivation of the electric model of the MALTA, two electrical angles, the linear electrical angle θ and the circumferential electrical angle φ are used, whose directions are also shown in **Fig. 3**.

The mechanical model is a nonlinear dynamic model, which allows to determine the mover's position (output of the model) depending on the total net forces \vec{v} that act on the mover (input of the model). The input of the mechanical model, the bearing and the drive force that act onto the MALTA mover are written in vector form as

$$\vec{v} = [f_{x,B1} \quad f_{y,B1} \quad f_{x,B2} \quad f_{y,B2} \quad f_D]^T \quad (1)$$

whose components are denoted in **Fig. 1**.

The position sensor model relates the center of gravity (COG) mover coordinates \vec{q}_t and \vec{q}_r (cf. equation (2)) to the displacements \vec{p} that are possible to measure with the position sensor planes SP1 and SP2 (cf. **Fig. 1**). The mass distribution of the mover is assumed to be even. Potential influence of the picked component mass in pick-and-place application is neglected, as the component mass is assumed to be much smaller than the mass of the mover (for example, this applies for SMD components to be mounted onto a printed circuit board in case of a pick-and-place application). For the derivation of the dynamic model, two coordinate reference frames, the inertial \mathcal{I} and the rotary \mathcal{R} reference frame (cf. **Fig. 3**) are used, which are described in more detail in the following subsection.

A. Nonlinear Dynamic Model of the Rigid Mover

The inertial reference frame \mathcal{I} is fixed to the origin \mathcal{O} and the $z_{\mathcal{I}}$ axis is oriented along the axial direction of the MALTA stator, whereas the rotary reference frame \mathcal{R} is fixed to the mover's center of gravity (COG) \mathcal{O}_{COG} and the $z_{\mathcal{I}}$ axis is aligned with its principal axis, as shown in **Fig. 4**. The tilting of the mover in **Fig. 4** is used to illustrate the position of the \mathcal{R} frame and it does not correspond to the tilting possible in reality. The motion of the mover is described in terms of *translation* and *rotation* of the frame \mathcal{R} with respect to the frame \mathcal{I} . The translation and rotation may be parametrized using a set of Cartesian coordinates \vec{q}_t and a set of Cardan angles \vec{q}_r as

$$\vec{q}_t = [x \quad y \quad z]^T, \quad \vec{q}_r = [\alpha \quad \beta \quad \gamma]^T. \quad (2)$$

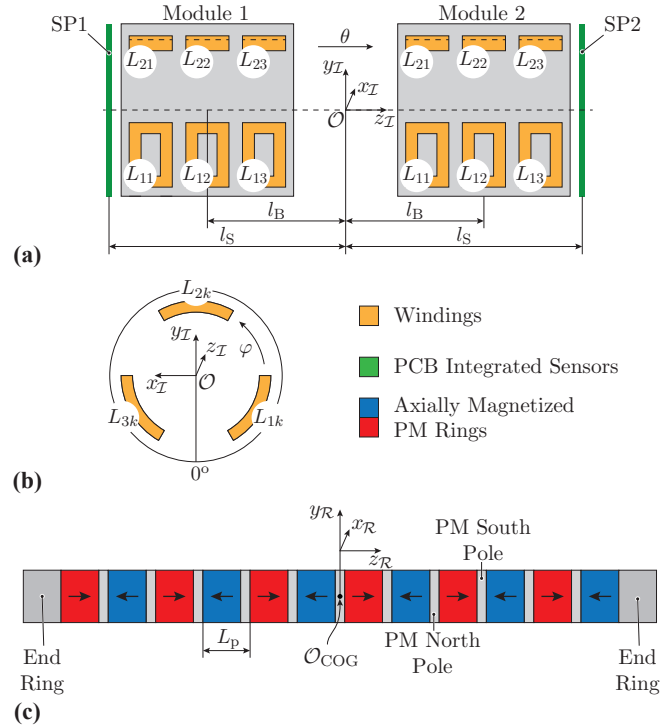


Fig. 3: Mechanical setup of the MALTA with inertial (\mathcal{I}) and rotary (\mathcal{R}) reference frames: (a) side view as denoted in **Fig. 1**; (b) front view on the sensor plane 1 (SP1) as denoted in **Fig. 1**; (c) mover construction showing the arrangement of the PMs and their flux density directions.

The angles in \vec{q}_r are three subsequent elementary rotations around the $x_{\mathcal{R}}$, $y_{\mathcal{R}}$ and $z_{\mathcal{R}}$ axes (cf. **Fig. 4**). Once the motion of the mover is parametrized, the equations of motion can be derived, for example by using the *Newton-Euler equations* [15], which can describe combined translation and rotation of a rigid body,

$$m \frac{\partial^2 \vec{q}_t}{\partial t^2} = \mathcal{I} \vec{F}_{tot} \quad (3)$$

$$\mathcal{R} \mathbf{I}_m \cdot \frac{\partial \mathcal{R} \vec{\omega}}{\partial t} + \mathcal{R} \vec{\omega} \times \mathcal{R} \mathbf{I}_m \cdot \mathcal{R} \vec{\omega} = \mathcal{R} \vec{T}_{tot},$$

where the translation is described in the inertial frame \mathcal{I} and the rotation in the rotary frame \mathcal{R} . \vec{F}_{tot} and \vec{T}_{tot} are the total force and the total torque acting on the mover, respectively. The mass of the mover is m , while $\mathcal{R} \mathbf{I}_m = \text{diag}(I_{xx}, I_{yy}, I_{zz})$ is the Moment of Inertia (MoI) diagonal matrix, expressed in the mover frame \mathcal{R} . The values of these parameters are given in the *Appendix*. The angular speed in the rotary frame \mathcal{R} is given by the following angular rotations

$$\mathcal{R} \vec{\omega} = \begin{bmatrix} 0 \\ 0 \\ \mathcal{I} \omega_z \end{bmatrix} + \mathbf{R}_z \begin{bmatrix} 0 \\ \mathcal{I} \omega_y \\ 0 \end{bmatrix} + \mathbf{R}_z \mathbf{R}_y \begin{bmatrix} \mathcal{I} \omega_x \\ 0 \\ 0 \end{bmatrix} \quad (4)$$

where $\mathcal{I} \omega_x = \partial \alpha / \partial t$, $\mathcal{I} \omega_y = \partial \beta / \partial t$, $\mathcal{I} \omega_z = \partial \gamma / \partial t$. Furthermore, a small angle approximation is used, i.e. for any angle ξ it applies $\sin \xi \approx \xi$ and $\cos \xi \approx 1$. The rotation matrices \mathbf{R}_y and \mathbf{R}_z are given in [16].

The total force on the mover is a superposition of the two net forces from the modules 1 and 2, acting at the points ${}_{\mathcal{I}} \vec{P}_1$ and ${}_{\mathcal{I}} \vec{P}_2$, which are in the middle of each module. These points are shown in **Fig. 4** and may be described analytically as

$${}_{\mathcal{I}} \vec{P}_1 = \begin{bmatrix} x - \beta(l_B + z) \\ y + \alpha(l_B + z) \\ -l_B \end{bmatrix}, \quad {}_{\mathcal{I}} \vec{P}_2 = \begin{bmatrix} x + \beta(l_B - z) \\ y - \alpha(l_B - z) \\ l_B \end{bmatrix}. \quad (5)$$

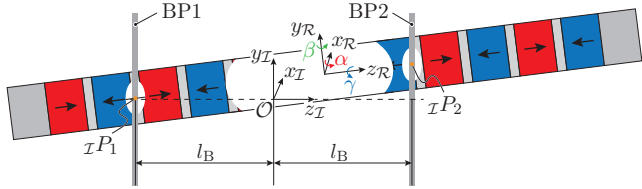


Fig. 4: Simplified mechanical setup showing the bearing planes 1 and 2 (BP1 and BP2) in the center of the modules 1 and 2, respectively (cf. **Fig. 3(a)**). The intersection points 1 and 2 are denoted by ${}_{\mathcal{I}}\vec{P}_1$ and ${}_{\mathcal{I}}\vec{P}_2$.

These expressions are derived from ${}_{\mathcal{I}}\vec{P}_1 = {}_{\mathcal{I}}\vec{O}_{\text{COG}} + \mathbf{R}_{\mathcal{I}\mathcal{R}} \mathcal{R}\vec{P}_1$ and ${}_{\mathcal{I}}\vec{P}_2 = {}_{\mathcal{I}}\vec{O}_{\text{COG}} + \mathbf{R}_{\mathcal{I}\mathcal{R}} \mathcal{R}\vec{P}_2$, where $\mathcal{R}\vec{P}_1 = [0 \ 0 \ (-l_B - z)]^\top$ and $\mathcal{R}\vec{P}_2 = [0 \ 0 \ (l_B - z)]^\top$. The 3×3 transformation matrix $\mathbf{R}_{\mathcal{I}\mathcal{R}} = \mathbf{R}_{\mathcal{R}\mathcal{I}}^{-1}$, where $\mathbf{R}_{\mathcal{R}\mathcal{I}} = \mathbf{R}_z \mathbf{R}_y \mathbf{R}_x$ (cf. [16]). Based on the position of these interaction points, the total forces and torques applied to the mover are discussed in the following.

1) *Total Force in Inertial Reference Frame:* The total force \vec{F}_{tot} acting on the mover consists of three force types: the drive, the bearing and the attraction force (also called *magnetic pull* or *detent* force). As the inertial frame \mathcal{I} is fixed to the stator, the total force may be readily expressed in the \mathcal{I} frame as ${}_{\mathcal{I}}\vec{F}_{\text{tot}}$, where ${}_{\mathcal{I}}\vec{F}_{\text{tot}}$ is composed of the two components coming from both modules 1 and 2, acting as a net force in the points ${}_{\mathcal{I}}\vec{P}_1$ and ${}_{\mathcal{I}}\vec{P}_2$,

$${}_{\mathcal{I}}\vec{F}_{\text{tot}} = {}_{\mathcal{I}}\vec{F}_1 + {}_{\mathcal{I}}\vec{F}_2. \quad (6)$$

The forces of each module, ${}_{\mathcal{I}}\vec{F}_1$ and ${}_{\mathcal{I}}\vec{F}_2$, are further split into a drive, a bearing and an attraction force type ${}_{\mathcal{I}}\vec{F}_1 = {}_{\mathcal{I}}\vec{F}_{D1} + {}_{\mathcal{I}}\vec{F}_{B1} + {}_{\mathcal{I}}\vec{F}_{A1}$ and ${}_{\mathcal{I}}\vec{F}_2 = {}_{\mathcal{I}}\vec{F}_{D2} + {}_{\mathcal{I}}\vec{F}_{B2} + {}_{\mathcal{I}}\vec{F}_{A2}$. It should be mentioned that these considered force vectors are analyzed in the Cartesian coordinate system (with the axes x , y and z) and, therefore, the vectors have a dimension of 3×1 .

The drive force component is an active component controlled by the drive currents in the stator and acts in the $z_{\mathcal{I}}$ axis direction. Therefore, it corresponds to the third component of the drive force vectors ${}_{\mathcal{I}}\vec{F}_{D1} = [0 \ 0 \ f_{D1}]^\top$ and ${}_{\mathcal{I}}\vec{F}_{D2} = [0 \ 0 \ f_{D2}]^\top$. The total drive force may be expressed as a superposition of the individual drive forces ${}_{\mathcal{I}}\vec{F}_{D1}$ and ${}_{\mathcal{I}}\vec{F}_{D2}$ as

$$\begin{aligned} {}_{\mathcal{I}}\vec{F}_D &= {}_{\mathcal{I}}\vec{F}_{D1} + {}_{\mathcal{I}}\vec{F}_{D2} \\ &= \begin{bmatrix} 0 \\ 0 \\ f_{D1} + f_{D2} \end{bmatrix}. \end{aligned} \quad (7)$$

The bearing forces are also actively controlled by the bearing current component in the stator windings. They act as net forces in $x_{\mathcal{I}}$ and $y_{\mathcal{I}}$ directions at the interaction points ${}_{\mathcal{I}}\vec{P}_1$ and ${}_{\mathcal{I}}\vec{P}_2$. Therefore, these forces constitute the first and the second component of the force vectors ${}_{\mathcal{I}}\vec{F}_{B1} = [f_{x,B1} \ f_{y,B1} \ 0]^\top$ and ${}_{\mathcal{I}}\vec{F}_{B2} = [f_{x,B2} \ f_{y,B2} \ 0]^\top$. The total bearing force may be expressed as a superposition of ${}_{\mathcal{I}}\vec{F}_{B1}$ and ${}_{\mathcal{I}}\vec{F}_{B2}$ as

$$\begin{aligned} {}_{\mathcal{I}}\vec{F}_B &= {}_{\mathcal{I}}\vec{F}_{B1} + {}_{\mathcal{I}}\vec{F}_{B2} \\ &= \begin{bmatrix} f_{x,B1} + f_{x,B2} \\ f_{y,B1} + f_{y,B2} \\ 0 \end{bmatrix}. \end{aligned} \quad (8)$$

The attraction forces are radial reluctance forces, which only generate a resulting attraction force on the mover if it is displaced from its center position, otherwise they cancel each other out. Thereby, it can be assumed that for a small

displacement the resulting attraction force acting at the interaction points ${}_{\mathcal{I}}\vec{P}_1$ and ${}_{\mathcal{I}}\vec{P}_2$ are proportional to the radial displacement at these points. Therefore, the modules 1 and 2 are producing the attraction forces ${}_{\mathcal{I}}\vec{F}_{A1} = K_A \cdot {}_{\mathcal{I}}\vec{P}_1$ and ${}_{\mathcal{I}}\vec{F}_{A2} = K_A \cdot {}_{\mathcal{I}}\vec{P}_2$ which can be written as

$${}_{\mathcal{I}}\vec{F}_{A1} = K_A \begin{bmatrix} x - \beta(l_B + z) \\ y + \alpha(l_B + z) \\ 0 \end{bmatrix}, \quad (9)$$

and

$${}_{\mathcal{I}}\vec{F}_{A2} = K_A \begin{bmatrix} x + \beta(l_B - z) \\ y - \alpha(l_B - z) \\ 0 \end{bmatrix}. \quad (10)$$

There, K_A equals the attraction constant per module, whose measured value of the prototype is given in **Tab. IV** in the *Appendix*. The total attraction force is then given as the superposition of the forces ${}_{\mathcal{I}}\vec{F}_{A1}$ and ${}_{\mathcal{I}}\vec{F}_{A2}$, i.e.

$${}_{\mathcal{I}}\vec{F}_A = {}_{\mathcal{I}}\vec{F}_{A1} + {}_{\mathcal{I}}\vec{F}_{A2}. \quad (11)$$

2) *Total Torque in Rotary Reference Frame:* By its magnetic design, the MALTA is designed as a linear motor (with integrated MBs). Therefore, it is not able to generate any drive torque (the torque around z -axis, which ‘drives’ the rotation of conventional rotary machines). Consequently, the total drive torque component is equal to zero. On the other hand, certain net forces (drive, bearing and attraction) may act on the mover at the interaction points ${}_{\mathcal{I}}\vec{P}_1$ and ${}_{\mathcal{I}}\vec{P}_2$ points, which may generate a certain net torque \vec{T}_{tot} on the mover. This net total torque is first determined in the \mathcal{I} frame, and then transformed into the \mathcal{R} frame.

In a first step, the lever arms are determined at the interaction points ${}_{\mathcal{I}}\vec{P}_1$ and ${}_{\mathcal{I}}\vec{P}_2$. The lever arms are vectors describing the distance between the force interaction point and the mover’s center of gravity \mathcal{O}_{COG} . In the inertial reference frame \mathcal{I} , for the MALTA mover two lever arms are defined as ${}_{\mathcal{I}}\vec{L}_1 = {}_{\mathcal{I}}\vec{P}_1 - {}_{\mathcal{I}}\mathcal{O}_{\text{COG}}$ and ${}_{\mathcal{I}}\vec{L}_2 = {}_{\mathcal{I}}\vec{P}_2 - {}_{\mathcal{I}}\mathcal{O}_{\text{COG}}$, which results in the following expressions

$${}_{\mathcal{I}}\vec{L}_1 = \begin{bmatrix} -\beta(l_B + z) \\ \alpha(l_B + z) \\ -l_B - z \end{bmatrix}, \quad {}_{\mathcal{I}}\vec{L}_2 = \begin{bmatrix} \beta(l_B - z) \\ -\alpha(l_B - z) \\ l_B - z \end{bmatrix}. \quad (12)$$

The net torques ${}_{\mathcal{I}}\vec{T}_1$ and ${}_{\mathcal{I}}\vec{T}_2$ produced by the MALTA modules 1 and 2, may be calculated then as

$${}_{\mathcal{I}}\vec{T}_1 = {}_{\mathcal{I}}\vec{L}_1 \times {}_{\mathcal{I}}\vec{F}_1, \quad {}_{\mathcal{I}}\vec{T}_2 = {}_{\mathcal{I}}\vec{L}_2 \times {}_{\mathcal{I}}\vec{F}_2. \quad (13)$$

Finally, the total torque acting on the mover in rotary \mathcal{R} reference frame is obtained as

$${}_{\mathcal{R}}\vec{T}_{\text{tot}} = \mathbf{R}_{\mathcal{R}\mathcal{I}}({}_{\mathcal{I}}\vec{T}_1 + {}_{\mathcal{I}}\vec{T}_2). \quad (14)$$

B. Position Sensor Model

In order to realize a closed-loop position control of the MALTA mover, the axial and radial positions have to be measured. There, it should be mentioned that the radial position has to be measured at two distinct axial locations, such that any tilting of the mover can be controlled. Therefore, two PCB integrated sensors are located at a certain distance l_S in z -direction from the origin \mathcal{O} of the inertial frame \mathcal{I} , as shown in **Fig. 3(a)**. The position measurement vector of SP1 and SP2 (which are denoted in **Fig. 1** and **Fig. 3**) may then be written as $\vec{p} = [x_1 \ y_1 \ x_2 \ y_2 \ z]^\top$, and the position of the mover described in terms of translation and rotation of the COG, may

be related to the measured positions as $\vec{p} = \mathbf{P}_0(z) [\vec{q}_t^\top \quad \vec{q}_r^\top]^\top$, where

$$\mathbf{P}_0(z) = \begin{bmatrix} 1 & 0 & 0 & 0 & -(l_S + z) & 0 \\ 0 & 1 & 0 & (l_S + z) & 0 & 0 \\ 1 & 0 & 0 & 0 & (l_S - z) & 0 \\ 0 & 1 & 0 & -(l_S - z) & 0 & 0 \\ 0 & 0 & 1 & 0 & 0 & 0 \end{bmatrix}, \quad (15)$$

can be deduced in analogy to the relations given in (5) for the two force interaction points, where in this case the measurement points l_S instead of l_B have to be used.

The hardware implementation of the two eddy-current sensors, which output a voltage that is proportional to the radial displacement, is shown in **Fig. 1** and **Fig. 11**. Hence, the two position sensors, denoted as SP1 and SP2 in **Fig. 3(a)**, can measure the radial positions of the mover at their axial locations $z = \pm l_S$, i.e. x_1 and y_1 are measured by SP1 at $-l_S$ and x_2 and y_2 are measured by SP2 at l_S . Furthermore, the axial position of the mover z is measured with Hall-effect sensors, as explained in **Sec. V-B**.

C. Electric Model

The drive force $\mathcal{I}\vec{F}_D$ and the bearing force $\mathcal{I}\vec{F}_B$, are controlled by the electric currents in the multiple three-phase windings of the MALTA, as shown in **Fig. 5(a)**. In conventional linear machines, the appropriate drive current to generate the desired thrust is typically obtained by performing a dq -transformation out of the three-phase currents in the axially arranged three-phase windings. The resulting q -current component is proportional to the generated thrust, and the resulting d -current component is used for field-weakening; however, it is typically controlled to zero.

For electric machines like the MALTA, which can also control the radial bearing forces on the mover (rotor), the same principle, i.e. the dq -transformation, can be applied to the radially arranged three-phase systems, whose obtained d - and q -current components directly control the resulting bearing forces in x - and y -direction. Hence, for electric machines which can either simultaneously generate drive and bearing forces or simultaneously rotate and move in linear direction, a dq -transformation for both systems should be applied, i.e. the rotational and the linear motion, which results in a so-called two-directional dq -transformation [17], [18]. Such a transformation has 4 components, dd , dq , qd and qq , where the components dq , qd may provide decoupled torque and axial force control (the first index is related to the rotation, while the second index corresponds to the linear motion, e.g. dq is the d -component for rotation and the q -component for the linear motion). As explained in [18], the MALTA drive current component is a zero-sequence component in rotary direction, and therefore, its q -component is denoted as $0q$ in the two-directional transformation, which is also shown in **Fig. 5(b)**. The bearing components have only d -component in axial direction and both d - and q -components in rotary direction, which gives dd - and qd -components for control of the bearing forces in x - and y -direction.

The MALTA drive and the bearing current components are separated from the 9-phase currents of each module by the

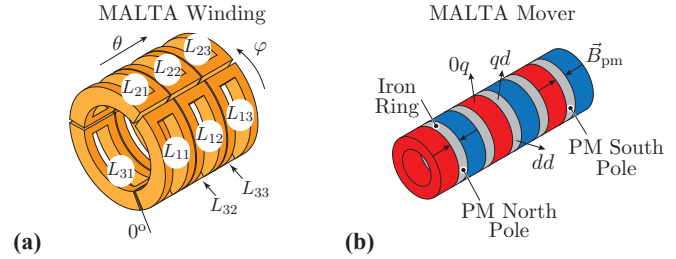


Fig. 5: Electrical system of the MALTA: **(a)** The winding system of a single module consisting of 9 concentrated coils. The complete MALTA prototype with module 1 and module 2 has $2 \times 9 = 18$ coils. **(b)** Mover with labelled two-directional dq -transformation axes (the first index for radial direction (bearing) and the second index for linear direction).

two-directional dq -transformation

$$\underbrace{\begin{bmatrix} x_{0d} & x_{0q} \\ x_{bd} & x_{bq} \end{bmatrix}}_{\mathbf{X}_{dq}} = \mathbf{K}_R(\varphi) \underbrace{\begin{bmatrix} x_{11} & x_{12} & x_{13} \\ x_{21} & x_{22} & x_{23} \\ x_{31} & x_{32} & x_{33} \end{bmatrix}}_{\mathbf{X}_{abc}} \mathbf{K}_L, \quad (16)$$

where x denotes any phase quantity (voltage, current or flux). The transformation matrices $\mathbf{K}_R(\varphi)$ and \mathbf{K}_L are given in [18]. The inverse transformation is derived from (16) by simply inverting the transformation matrices $\mathbf{X}_{abc} = \mathbf{K}_R^{-1}(\varphi) \mathbf{X}_{dq} \mathbf{K}_L^{-1}$.

The drive (propulsion) force of both modules is controlled by the q -component of the drive current i_{0q} . Therefore, for the modules 1 and 2 the drive force components are

$$f_{D1} = K_D i_{0q1}, \quad f_{D2} = K_D i_{0q2}, \quad (17)$$

where f_{D1} and f_{D2} are part of the $\mathcal{I}\vec{F}_D$ force vector from the mechanical model given (7) and K_D is the MALTA drive constant. The drive constant value is measured in [11] and its value is given in **Tab. IV** in the *Appendix*.

The bearing force components are controlled with the bearing current components as

$$f_{B1} = K_B i_{bd1}, \quad f_{B2} = K_B i_{bd2}, \quad (18)$$

where $f_{B1} = \sqrt{f_{x,B1}^2 + f_{y,B1}^2}$ and $f_{B2} = \sqrt{f_{x,B2}^2 + f_{y,B2}^2}$. The force components $f_{\{x,y\}B\{1,2\}}$ are part of the $\mathcal{I}\vec{F}_B$ force vector from the mechanical model given in (8) and K_B is the bearing constant whose value is measured and given in **Tab. IV** in the *Appendix*. It should be noted in (18) that only the amplitude of the bearing force is controlled. The direction of the bearing force control is achieved by commanding the angle φ in the transformation (16) for modules 1 and 2 as $\varphi_1 = \text{atan2}(f_{y,B1}/f_{x,B1})$ and $\varphi_2 = \text{atan2}(f_{y,B2}/f_{x,B2})$, respectively.

III. MALTA MECHANICAL MODEL LINEARIZATION

The nonlinear mechanical model given with the equations of motion (3), together with the model of the position sensor and the electrical model, may be used for numerical simulation of the MALTA dynamics. To use the nonlinear mechanical model for the position controller design, the model is linearized at first. The linearization is performed around the steady-state point $\vec{q}_{ss} = [x = 0 \quad y = 0 \quad z = z_{ss} \quad \alpha = 0 \quad \beta = 0 \quad \gamma = 0]^\top$. At the steady-state point, the mover can be displaced in axial direction, but should be in the radial center and not tilted. The performed linearization results in a system of 6 linear differential equations. At this point, since rotation of the MALTA mover can not be actively controlled, the last equation that describes

TABLE I: Poles (eigenvalues) of the linearized MALTA system.

Symbol	Mode	Eigenvalue
$\lambda_{1,2}$	x	± 218.92
$\lambda_{3,4}$	y	± 218.92
$\lambda_{5,6}$	z	0
$\lambda_{7,8}$	α	± 157.53
$\lambda_{9,10}$	β	± 157.53

the dynamics of the angle γ is removed from the further analysis. This gives a system of 5 linear differential equations, which can be written in a vector form as $\mathbf{M}(\partial^2 \vec{q}/\partial t^2) = \mathbf{S}\vec{q} + \mathbf{V}\vec{v}$ and represent *linearized equations of motion*. The position vector is equal to $\vec{q} = [x \ y \ z \ \alpha \ \beta]^\top$ and the input vector is $\vec{v} = [f_{x,B1} \ f_{y,B1} \ f_{x,B2} \ f_{y,B2} \ f_D]^\top$, where $f_D = f_{D1} + f_{D2}$, cf. (17). Due to limited space, matrices \mathbf{M} , \mathbf{S} and \mathbf{V} are not shown.

The most favorable form of the MIMO system for the controller design is the state-space form of the linear equations, where the first derivatives of the states are expressed as functions of the states itself and the inputs (drive and bearing forces). In order get the state-space form, the second derivatives from the linearized equations of motions are removed by augmenting the state vector as $\vec{\xi} = [\vec{q} \ \partial \vec{q}/\partial t]^\top$, which gives the system in a standard state-space form

$$\begin{aligned} \frac{\partial \vec{\xi}}{\partial t} &= \mathbf{A}_{10 \times 10} \vec{\xi} + \mathbf{B}_{10 \times 5} \vec{v}, \\ \vec{p} &= \mathbf{C}_{5 \times 10} \vec{\xi}, \end{aligned} \quad (19)$$

The second equation in (19) is the output equation, where $\mathbf{C} = [\mathbf{P}_{5 \times 5}(z_0) \ \mathbf{0}_{5 \times 5}]$. The matrix $\mathbf{P}_{5 \times 5}(z_0)$ is obtained from (15) by removing the last column and $\mathbf{0}_{5 \times 5}$ is the zero matrix.

From the linearized state-space system representation (19), the poles of the system are determined as the eigenvalues of the matrix \mathbf{A} , which are given in **Tab. I** for the case $z_{ss} = 0$. The linearization was also studied for $z_{ss} \in [-15, 15]$ mm, revealing that the pole locations do not vary significantly. The system is open-loop unstable, since there exist positive poles. These are caused by the destabilizing attraction forces, which act on the mover in a ‘negative-stiffness spring’ fashion. The largest unstable pole imposes a minimum requirement on the closed-loop bandwidth of the position control system (as a rule of thumb, the closed-loop system bandwidth should be twice the frequency of the largest unstable pole [19]). For example, from **Tab. I** the largest frequency is $218.92 \text{ rad s}^{-1}$ and it is associated to the unstable pole $\lambda_1 = 218.92$.

IV. CONTROLLER DESIGN

The overall MALTA control scheme is presented in **Fig. 6**. It features a cascaded structure, with the inner current control loop and the outer position control loop. This is a common choice for control of electromechanical actuators as the mechanical time constants are typically much greater than the electrical ones, thus exhibiting a dynamic separation in frequency domain. This allows independent design of the outer, slower control loop and the inner, faster one. In the following, first the position controller and hence the current controller are described.

A. Position Controller

For the outer position loop a COG control strategy [12] is chosen, which consists in controlling position and orientation

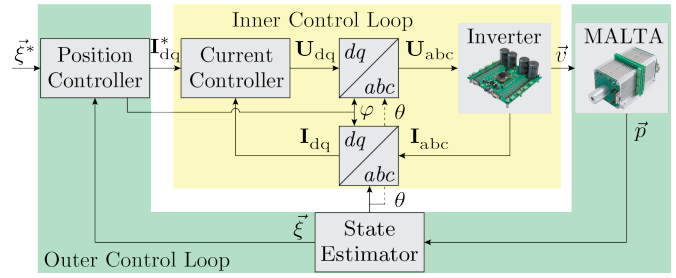


Fig. 6: Overview of the cascaded MALTA control structure. The current controller is in the inner control loop, while the position controller is in the outer control loop.

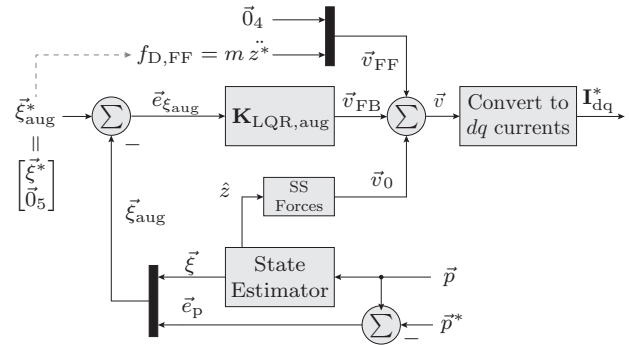


Fig. 7: Structure of the MALTA position controller. From the output measurements \vec{p} , the state $\vec{\xi}$ is estimated with the state estimator (Kalman Filter) and used for LQR feedback control. To enhance performances, the feedforward force commands \vec{v}_{FF} (for tracking) and \vec{v}_0 (steady-state compensation) are added to the feedback-only component \vec{v}_{FB} obtaining the total force command \vec{v} . This is finally converted into the desired dq currents i^{dq*} .

of the mover frame \mathcal{R} , rather than axial and radial positions \vec{p} sensed at the sensor planes (i.e. output control or *decentralized* approach). As COG coordinates \vec{q} make part of the state of the system $\vec{\xi}$, a multi-input multi-output (MIMO) Linear Quadratic Regulator (LQR) [20] based on *full state feedback* is ultimately chosen. Given the state error signals \vec{e}_{ξ} , computed as the difference from the state reference $\vec{\xi}^*$ and the current state $\vec{\xi}$, the controller provides the force commands \vec{v}_{FB} to apply to the mover. The complete structure of the position controller is shown in **Fig. 7**.

The current state $\vec{\xi}$ is estimated from the output measurements \vec{p} with a state observer. A *steady-state Kalman Filter*, a particular form of the more general Luenberger observer, is chosen. The (Kalman) gain of the observer is obtained by solving a quadratic optimization problem which corresponds to the dual problem of LQR control. The design weights \mathbf{Q}_{obs} and \mathbf{R}_{obs} are obtained from the variances of the process and sensor noise, respectively, which are assumed to be normally distributed. Their values, given in **Tab. II(a)**, are determined from open-loop measurements in order to prevent correlation of the two kinds of noise. As without feedback control the mover cannot levitate, position sensors are statistically characterized with no phase currents, i.e. with the mover resting on the touchdown bearing. Concerning input forces, it is equivalent to statistically characterize input currents, as they are directly proportional. In this case the mover is removed from the machine and DC currents of 1 A in dq -frame for the bearing and the drive force generation are applied (cf. (17) and (18)). This way, the variances in **Tab. II(a)** are obtained.

It should be mentioned that a state observer is not mandatory

for COG control. In fact, in most AMBs setups the measurement matrix is square and invertible. Hence, it is possible to explicitly map measurements back into COG coordinates as $\vec{q} = \mathbf{P}_0^{-1}(z)\vec{p}$. For the MALTA, as $\mathbf{P}_0(z)$ in (15) is not invertible, the Moore-Penrose pseudoinverse $\mathbf{P}_0^\dagger(z)$ should be used instead. Nevertheless, the use of the (full) state estimate for feedback control is advantageous. Not only it allows filtering out noise from measurement data in an optimal sense, but also it provides speed estimates, which can be used to implement derivative control action. This is highly beneficial, as it avoids the direct computation of discrete derivatives from the measurement data, which would result in noise amplification for noisy signals.

The LQR position controller is tuned by choosing the design weights \mathbf{Q} and \mathbf{R} as reported in **Tab. II(b)**. LQR design often includes some trial and error, as it is a matter of trade-off between penalization of large state or large input magnitudes. In this case, in order to gain some insight on the closed loop system, the controller is tuned iteratively by shaping the singular value decomposition of the complementary sensitivity function (i.e. the closed loop transfer function), using the established linearized dynamic model.

The modes x and y , as well as α and β are tuned in the same way, whereas different weights are chosen specifically for z . With these choices, the resulting MIMO position controller closed-loop bandwidth is around 400 rad s^{-1} . To further increase the bandwidth of the position controller, an increased bandwidth of the inner current controller is required such that dynamic decoupling between the inner and outer control loops is guaranteed.

In order to suppress steady-state errors and provide responsive disturbance rejection, integral action is added to the position controller. The levitated mover is originally modelled as a pure double integrator. This would make the loop gain *type 2* (i.e. with 2 poles in the origin), which implies that both step and ramp responses can already be tracked with zero steady state error. However, this would be only an ideal condition. In practice, additional physical phenomena impact the levitated mover, such as cogging force, with the result that the two poles are moved away from the origin. Therefore, additional integral action is required. This is included in the LQR design by augmenting the state as $\vec{\xi}_{\text{aug}} = \begin{bmatrix} \vec{\xi} & \vec{e}_p = \vec{p}^* - \vec{p} \end{bmatrix}^\top$, i.e. by adding the output error dynamics to the state and regulating it to zero. The LQR design weights for the augmented system become then as in **Tab. II(c)**.

The performances of the position controller are enhanced with feedforward components \vec{v}_{FF} , which are added directly after feedback control action computation. More specifically, feedforward control is provided along the axial direction z in order to improve transient responses to known references. This is possible with an appropriate force component $f_{\text{D,FF}}$ obtained through inversion of the plant's dynamics. If z^* is the axial position reference to be tracked, then $f_{\text{D,FF}} = m \ddot{z}^*$. With the feedforward component, the controller knows in advance how to act to follow the commanded reference, instead of reacting after it has already changed. This allows speeding up transient response and tracking faster references, leveraging the feedback part from this task. The feedforward control in radial direction may be provided via the first four

TABLE II: LQG Control weights: (a) LQR control, (b) LQR augmented control, (c) SS-KF observer.

$\mathbf{Q}_{\text{obs}} = \mathbf{B} \text{diag}(\sigma_{fx1}^2, \sigma_{fy1}^2, \sigma_{fx2}^2, \sigma_{fy2}^2, \sigma_{fz}^2) \mathbf{B}^\top$			
$\mathbf{R}_{\text{obs}} = \text{diag}(\sigma_{x1}^2, \sigma_{y1}^2, \sigma_{x2}^2, \sigma_{y2}^2, \sigma_z^2)$			
$\sigma_{x1}^2, \sigma_{x2}^2$	$7.06 \cdot 10^{-10}$	$\sigma_{fx1}^2, \sigma_{fx2}^2$	$2.5 \cdot 10^{-3}$
$\sigma_{y1}^2, \sigma_{y2}^2$	$4.53 \cdot 10^{-10}$	$\sigma_{fy1}^2, \sigma_{fy2}^2$	$2.5 \cdot 10^{-3}$
σ_z^2	$1.55 \cdot 10^{-8}$	σ_{fz}^2	$4.9 \cdot 10^{-3}$

(a)

$\mathbf{Q} = \text{diag}(q_x, q_y, q_z, q_\alpha, q_\beta, q_{dx}, q_{dy}, q_{dz}, q_{d\alpha}, q_{d\beta})$			
$\mathbf{R} = \text{diag}(r_{fx1}, r_{fy1}, r_{fx2}, r_{fy2}, r_{fz})$			
q_x, q_y	3.25	q_{dx}, q_{dy}	10
q_α, q_β	15	$q_{d\alpha}, q_{d\beta}$	12
q_z	0.3	q_{dz}	0.3
		r_{fx1}, r_{fy1}	1
		r_{fx2}, r_{fy2}	1
		r_{fz}	0.1

(b)

$\mathbf{Q}_{\text{aug}} = \text{diag}(\mathbf{Q}, q_{ex1}, q_{ey1}, q_{ex2}, q_{ey2}, q_{ez})$	
q_{ex1}, q_{ey1}	80
q_{ex2}, q_{ey2}	80
q_{ez}	30

(c)

components of \vec{v}_{FF} , which can be used to counter any known radial disturbances, e.g. when the MALTA is moved with parallel kinematics in pick-and-place robots.

The feedforward action includes an additional component $\vec{v}_0(z)$ to adjust in advance steady-state forces according to the current axial position z . These include for example gravity compensation with the two bearing forces $f_{y,B1}$ and $f_{y,B2}$ and compensation of irregularities in the radial pull forces due to asymmetries and manufacturing tolerances. Nevertheless, the feedforward steady-state action $\vec{v}_0(z)$ includes also a linear (axial) cogging force component, which is already passively significantly reduced to a very low values by choosing a distance between the two MALTA stator modules that minimizes it. These components are recorded from the position controller reference signal in steady-state.

It is of interest to investigate whether manufacturing tolerances and uncertainties in the system may compromise the stability of the designed position controller. This is even more relevant, as in pick-and-place applications the mass of the mover varies according to the picked object. For this reason, the LQR design is tested for robust stability in MATLAB. By allowing a 20% uncertainty on m, K_A, K_D and K_B , the system is expected to tolerate up to around 300% of the modeled uncertainty. In the case of the mass m , this means that the expected maximum payload is around 0.2 kg. Nevertheless, in pick-and-place of e.g. electronic components, the payload mass could even be neglected as it is much smaller than the mover's mass, as already mentioned in **Sec. II**.

The total control forces are finally converted into the appropriate dq currents responsible for force generation, as discussed in **Sec. II-C**, cf. (17) and (18).

B. Current Controller

The structure of the current controller is shown in **Fig. 8**. The control actions are the dq -voltages \mathbf{U}_{dq} , which are transformed into the phase voltages \mathbf{U}_{abc} according to the transformation introduced in **Sec. II-C**. These are finally converted into equivalent duty cycles \mathbf{d}_{abc} for pulse-width modulation. The switching frequency of the MALTA inverter is $f_{\text{sw}} = 100 \text{ kHz}$.

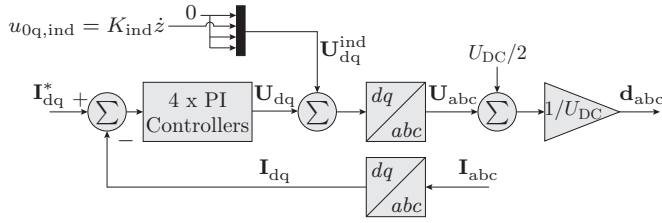


Fig. 8: Structure of the MALTA current controller. Only one module is considered for simplicity. There are 4 dq quantities to be controlled: i_{0d} , i_{0q} , i_{bd} , and i_{bq} . Hence, 4 PI-controllers, all designed and tuned in the same way, are used.

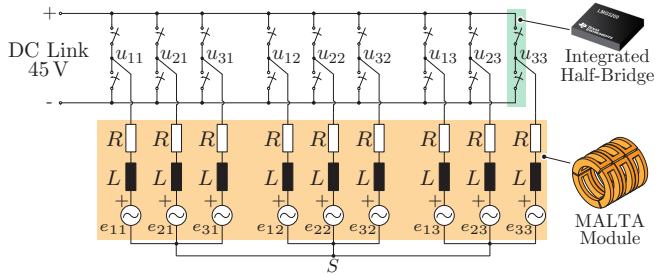


Fig. 9: Power circuit schematic of a single MALTA stator module supplied by the 45 VDC inverter. The resistance and the inductance of a phase winding are $R = 2.2 \Omega$ and $L = 2.8 \text{ mH}$. The induced voltages $e_{\{1,2,3\}\{1,2,3\}}$ have the amplitude equal to $K_{\text{ind}} \cdot v_z$, where $K_{\text{ind}} = \pi \Psi / L_p = 1.74 \text{ Vs/m}$, $\Psi = 8.3 \text{ mWb}$ is the flux linkage, $L_p = 15 \text{ mm}$ is the pole size and v_z is the linear mechanical speed of the MALTA mover.

The current controller is designed using the linearized steady-state electrical model in stationary dq coordinates, i.e. with $\dot{\varphi} = 0$ and $\dot{\theta} = 0$. The model is of the form

$$\frac{di_k(t)}{dt} = -\frac{R_k}{L_k} i_k(t) + \frac{1}{L_k} u_k(t), \quad (20)$$

where $k \in \{0d, 0q, bd, bq\}$ denotes the stationary coordinate axes, cf. **Fig. 5(b)**. The PI current controllers are tuned such that the crossover frequency is $\omega_c^{\text{cc}} = 3000 \text{ rad s}^{-1}$, which is considerably higher than the crossover frequency of the position controller. The phase margin is 60° to ensure an acceptable overshoot of the transient response. The voltages u_{0q1} and u_{0q2} also include an additional feedforward correction factor $u_{0q,\text{ind}} = K_{\text{ind}} \dot{z}$, to compensate for the induced voltage due to non-zero linear speed along the z axis during operation, cf. **Fig. 9**.

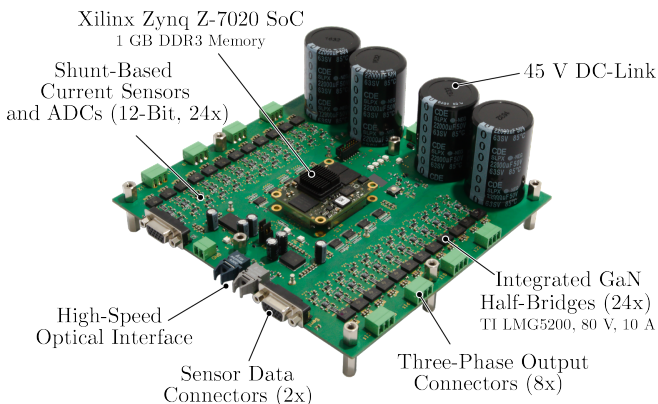


Fig. 10: Two-level MALTA inverter, which consists of 24 chip integrated half-bridges, control board and digital interfaces for position sensors. The power circuit schematic for a single MALTA module is shown in **Fig. 9**.

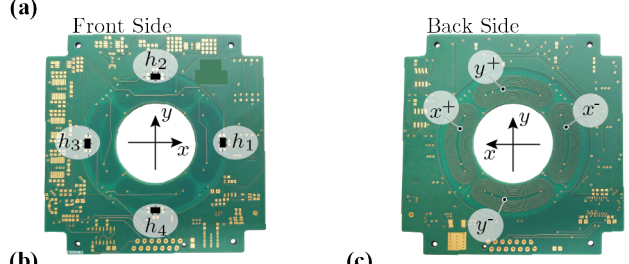
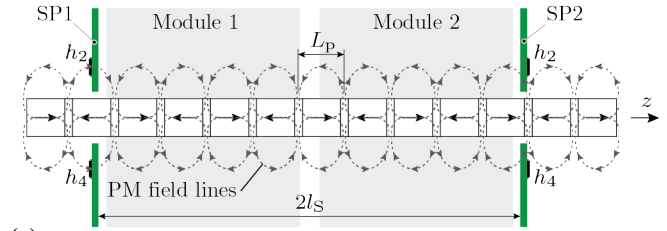


Fig. 11: (a) Illustration of the PM field lines used to sense the axial position of the mover and the sensor planes SP1 and SP2, at axial distance $2l_s$. (b) Front side of the sensor prototype with four Hall-effect sensors, denoted as h_1 , h_2 , h_3 and h_4 . The Hall-effect sensors can sense z component (axial) of the PM field. The displacement $2l_s$ is such that the sensed PM field from SP1 and SP2 Hall sensors is shifted by a half the PM pole size $L_p/2$. (c) Back side of the PCB integrated sensor prototype. The eddy current sensor coils for x direction (x^+ , x^-) are connected in anti-series, as well as (y^+ , y^-) for y direction. The physical size of sensor PCBs is $8 \times 8 \text{ cm}$.

V. HARDWARE REALIZATIONS OF INVERTER SUPPLY AND POSITION SENSOR

A. MALTA Inverter Supply

The control system is discretized (with the *backward Euler* method) and implemented in C code on the employed high-performance digital signal processing platform (*Xilinx Zynq Z-7020*, cf. **Fig. 10**). It is executed at a rate of 20 kHz , which is limited by the available processing capability. The 18 integrated gallium nitride (GaN) half-bridges (*Texas Instruments LMG5200*) required to drive the MALTA are controlled by 18 individual pulse-width modulators implemented in the fabric of the FPGA processing platform.

In MALTA operation, the mover exhibits accelerations and decelerations, which reflects onto the electrical part of the system by consumption or generation of electrical energy that might cause oscillations of the DC-link voltage. Therefore, a rather large capacitance of $4 \times 22 \text{ mF} = 88 \text{ mF}$ is used in the DC-link. For example, if the mover has a linear speed of 5 m/s , it has accumulated kinetic energy of $0.5 \cdot 0.36 \text{ kg} \cdot (5 \text{ m/s})^2 = 4.5 \text{ J}$. If the losses in the inverter and the MALTA are neglected, this kinetic energy will be added to the electric energy in the DC-link caps and would cause a voltage oscillation of $\sim 1.12 \text{ V}$, which is around 2.5% of the 45 VDC and it is an acceptable value. This issue could be also addressed by e.g. adding a braking resistor in the DC-link, which would allow to use a lower DC-link capacitance value.

B. MALTA Position Sensor

The MALTA position sensors are realized on PCBs (cf. **Fig. 1**) and placed with respect to the stator modules as shown in **Fig. 11(a)**. For the axial position detection, the signals from the Hall-effect sensors located on both sensor planes, SP1 and SP2, are used. This is a very well known method where 'sin'

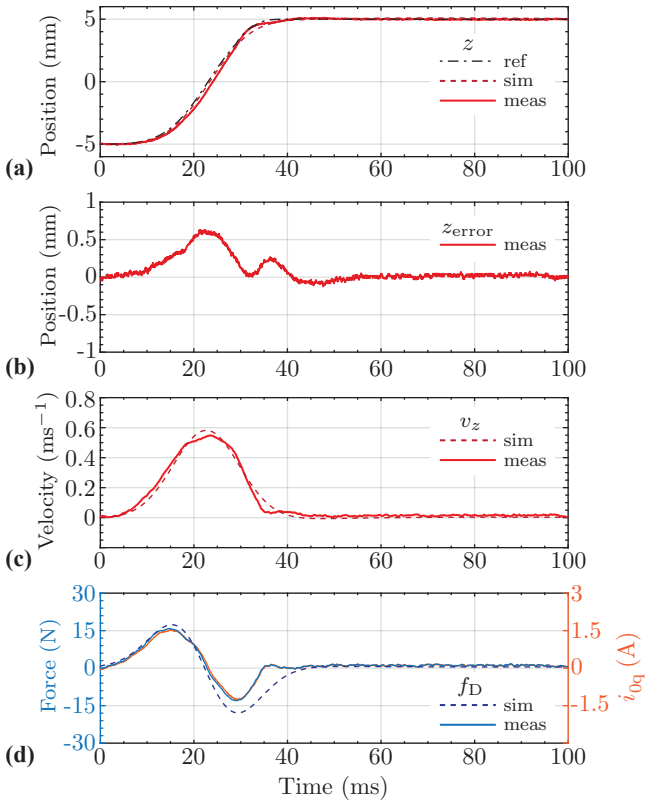


Fig. 12: Measurements of the MALTA response for a 10 mm axial stroke. (a) Reference axial position, simulation and actual response. The reference for z , shown as a black dashed line, is shaped with a sigmoid profile to improve tracking performances. The actual z response is shown in red and it tracks the reference with 16.2 ms rise time and $\leq 1.5\%$ overshoot. (b) Axial position tracking error stays below 0.6 mm (c) Axial speed profile. (d) Axial driving force (total) and correspondent dq component (only for Module 1). It is possible to verify the value of the drive constant of $K_D \approx 5 \text{ N A}^{-1}$.

and ‘cos’ of the PM field need to be measured such that linear position can be detected [21]. In conventional linear machines where the radial position of the mover is governed, e.g. by mechanical bearings, the PM field sensed by the Hall-effect sensors can change only if the mover moves in linear z -direction. Since in the MALTA, the mover is capable also to move radially (for the MALTA from approx. -0.6 mm to 0.6 mm), which is allowed by the integrated MBs, the change of the PM field detected by the Hall-effect sensor due to radial motion can not be differed from the PM field change due to linear motion, which may lead to an inaccurate linear position detection. Therefore, for the linear position detection of the MALTA, the ‘sin’ and ‘cos’ signals are formed by the average sum of the four Hall-effect sensors, i.e. $(h_1 + h_2 + h_3 + h_4)/4$. This mitigates the sensitivity of the sensed PM field change to the radial motions of the MALTA mover. For example, if the mover moves in the positive y direction (cf. Fig. 11(b)), the PM field sensed by h_2 would increase while the field for h_4 reduces, i.e. their average sum stays approximately constant. Finally, in total 8 Hall-effect sensors (4 per sensor plane) are used for the linear position detection of the MALTA’s mover.

The radial position is detected by the PCB integrated eddy current position sensor, shown in Fig. 11(c). Detailed explanation about the sensor operating principles and its equivalent circuit may be found in [22], [23].

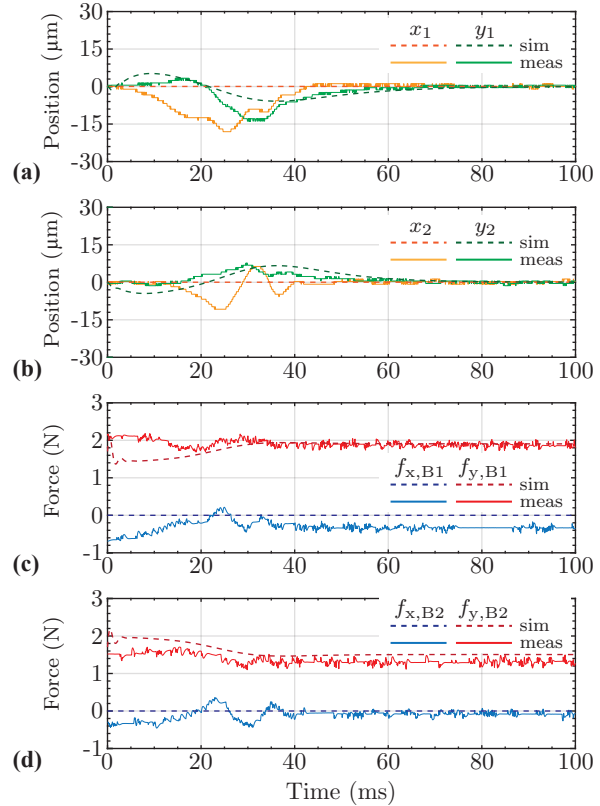


Fig. 13: Measurements of the MALTA response for a 10 mm axial stroke corresponding to Fig. 12. (a-b) Radial responses in x and y directions for Module 1 and Module 2. The maximum deviation is contained within $\pm 20 \mu\text{m}$. According to simulation of the dynamical model, deviations y_1 and y_2 are expected, whereas this is not the case for x_1 and x_2 . This mismatch can be explained by manufacturing tolerances. (c-d) Commanded forces from the position controller for Module 1 and Module 2. $f_{y,B1}$ is larger than $f_{y,B2}$ at steady-state as the mover is unbalanced towards Module 1. Their sum compensates the gravity force $m \cdot g \approx 3.25 \text{ N}$.

VI. MEASUREMENT RESULTS

The shown measurements are conducted on the MALTA prototype with the controller structure described in Sec. IV. In order to get the shown position controller performance, the MALTA prototype was fixed in a stable test-bench where the commissioning of the MALTA prototype (force and attraction constants measurements, cf. Tab. IV) and position sensor is done, which data is then used in the implemented controller, either in the form of the constant parameter (cf. Tab. IV) or the lookup table (cf. \vec{v}_0 in Fig. 7).

A. Axial Reference Tracking

The experimental setup of the MALTA actuator and its inverter are shown in Fig. 1 and Fig. 10, respectively. In order to demonstrate the operation of the MALTA, an axial 10 mm stroke is commanded to the position controller as shown in Fig. 12(a). The non-zero steady-state force/current that can be observed in Fig. 12(d) from around 40 ms onwards is needed to counteract the cogging force, guaranteeing average steady-state errors in the order of $1 \mu\text{m}$ (cf. also Tab. III). Due to feedforward control, the controller tracks the assigned sigmoid position reference z without overshooting, which is seen from the measurements in Fig. 12(a).

In Fig. 13, the radial position responses to the same axial step of Fig. 12(a) are shown. The radial position control rejects effectively the disturbances occurring during fast axial motion,

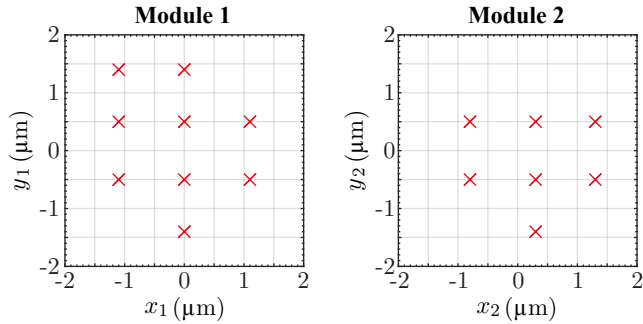


Fig. 14: Measurement distribution of the steady-state radial positions of the Module 1 and Module 2. Axial position reference is $z^* = 0$, i.e. mover is in the middle. From the 2000 samples, sensor resolution is clearly visible to be around $1\ \mu\text{m}$.

maintaining the deviations within $\pm 20\ \mu\text{m}$ (cf. **Fig. 13(a),(b)**). In **Fig. 13(c),(d)** the commanded radial forces are shown. Also in this case, after reaching steady-state they have a non-zero value. In particular, $f_{y,B1}$ and $f_{y,B2}$ are needed to keep the mover levitated and their sum corresponds in fact to $mg \approx 3.25\ \text{N}$. As the mover is unbalanced towards the first stator module (at the steady-state axial position of $5\ \text{mm}$), $f_{y,B1}$ is larger than $f_{y,B2}$. It should be mentioned that additional unknown radial disturbances, e.g. external vibrations, could cause higher radial position deviations.

In both **Fig. 12** and **Fig. 13** the dashed lines are the simulated responses to the same smooth reference as obtained from a MATLAB Simulink model. This is built according to the modelling of **Sec. II**, derived from first physical principles. By allowing for the expected differences between model and measurements due to manufacturing tolerances, unmodeled dynamics and noise, it can be assessed that the two are in good agreement. An exception are the measured x_1 and x_2 positions, which according to the model should not be affected by an axial motion. This mismatch can be explained both with the irregular magnetic field distribution inside the two stator modules and tolerances in the strengths of the permanent magnets of the mover.

B. Steady-State Positioning Performance

Positioning performances in steady-state may be further investigated with the measurements shown in **Fig. 14**, for the case of $z^* = 0$ (mover in the middle). It can be clearly seen that the measured radial positions are very close to the sensor resolution of $\approx 1\ \mu\text{m}$. This is a good result offered by the chosen eddy current sensor technique. **Tab. III** finally summarizes the statistical metrics of all the measured position signals. The noticeably higher variance of the axial z position is due to the Hall-effect sensor technique employed, which is more prone to noise.

TABLE III: Statistical metrics (mean and standard deviation (STD)) of the steady-state position measurements calculated from 2000 measured samples.

Position (Symbol)	Mean (μm)	STD (μm)	Motion Range (μm)
Axial (z)	-0.5224	15.4277	$\pm 15 \times 10^3$
Module 1			
x -direction (x_1)	0.0335	0.3883	± 600
y -direction (y_1)	-0.0212	0.5579	± 600
Module 2			
x -direction (x_2)	0.0579	0.4827	± 600
y -direction (y_2)	-0.0735	0.4956	± 600

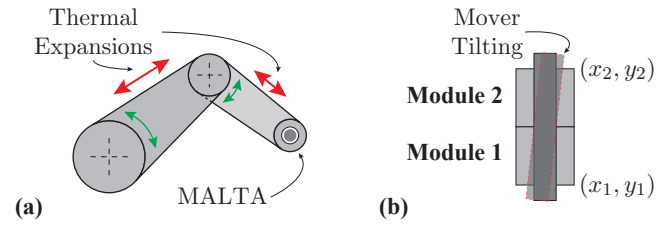


Fig. 15: (a) Setup of a typical application with MALTA mounted as an end-effector of a robot arm. If the robot arm experiences thermal expansions during operation, the overall precision of the positioning system is compromised. (b) The active tilting and radial control to provide an appropriate correction of the compromised position.

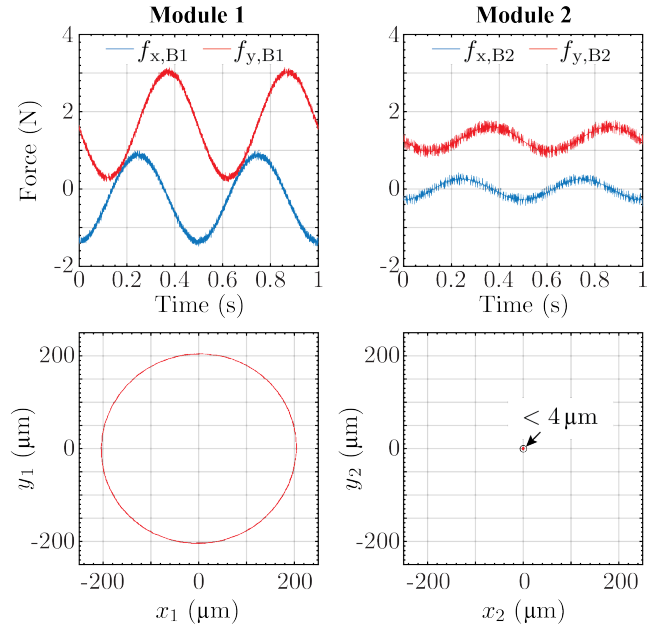


Fig. 16: Measurements of the mover tilting control. The assigned reference is given with the expression (21).

C. Mover Tilting Capability

A special characteristic of the MALTA system is the possibility of actively controlling the tilting of the mover, cf. **Fig. 15**. This can be exploited for advanced positioning systems. For instance, in a typical application, an actuator like the MALTA would be mounted as an end-effector of a robotic arm, cf. **Fig. 15(a)**, for instance in a pick-and-place robot application. If during the operation the whole setup heats up, thermal expansions of the supporting robotic arm occur. For example, a robotic arm of $0.5\ \text{m}$ length would extend in length for around $\approx 65\ \mu\text{m}$, if the temperature rises for $10\ ^\circ\text{C}$ (temperature expansion coefficient of steel equal to $13 \times 10^{-6}\ ^\circ\text{C}^{-1}$ is assumed). This would totally compromise precise positioning of the end-effector if no correction is applied. However, with the MALTA, these thermal disturbances may be completely decoupled by active magnetic bearings and the radial precision is determined by the precision of the radial eddy-current position sensor. The thermal expansions may be measured, e.g. by measuring the position of the MALTA mover with a laser sensor mounted on a support that is not affected by the thermal expansions. This feature may justify an effort of integrating MBs into the actuators, as some of the conventional solutions have water cooling systems in the robotic arms, which limit temperature changes and thermal expansions.

This concept is demonstrated with the experiment shown in

Fig. 16. In this case, a circumference of radius $S = 200 \mu\text{m}$ is assigned as a reference to be tracked along the SP1 plane, whereas the mover should be kept fixed at the center of the SP2. The reference

$$\bar{p}^*(t) = [S \cos(2\pi f_{p^*} t) \quad S \sin(2\pi f_{p^*} t) \quad 0 \quad 0 \quad 0]^\top \quad (21)$$

is then directly used for integral control and transformed into the appropriate state reference $\xi^* = [\bar{q}^* \quad \partial \bar{q}^* / \partial t]^\top$, with $\bar{q}^* = \mathbf{P}_0^{-1}(z) \bar{p}^*$ for full state feedback. The controller is employed to track the circumference at $f_{p^*} = 2 \text{ Hz}$. The measurements in **Fig. 16** show the response of the system for both modules. It can be seen how the radial motions in the Module 1 affect the Module 2, where the controller commands the forces $f_{x,B2}$ and $f_{y,B2}$ that keep the radial position deviation from the reference center position below $4 \mu\text{m}$.

VII. CONCLUSION

In this paper, dynamic operation of the Magnetically Levitated Tubular Actuator (MALTA) is analyzed. The analysis starts with the dynamic mechanical modeling of the MALTA system by using Newton-Euler equations that may describe combined translation and rotation of the MALTA rigid mover. Each of the force types (drive, bearing or attraction) that act on the mover are modeled, as well as the torques that they create. As the mover position is described by the translation and rotation of its center of gravity and the position sensor provides measurements of the radial and axial positions, sensor system is modeled and mapping with the center of gravity coordinates is given. Control system is LQR feedback controller assisted with the feed-forward compensation of the nonlinearities due to the cogging force and the induced voltage due to linear motion. It has cascaded structure with inner (faster) current control loop and outer position control loop. Additionally, a mechanical model based observer is designed, which is used to provide information about the states and state derivatives (speeds) such that high-frequency noise amplification due to measurement signal differentiation is avoided. In the measurement experiments, MALTA system shows good axial reference tracking with the 10 mm axial stroke amplitude and 16.2 ms of the rise time. During this axial movement, the mover deviation from its center is below $20 \mu\text{m}$. By studying statistical metrics of the controlled positions in the steady-state, the radial positions exhibit standard deviation around $0.5 \mu\text{m}$ and the axial position around $15 \mu\text{m}$. In the final measurement experiment an application example is proven, in which the mover tilting control of the proposed MALTA is used to compensate for any thermal expansions that would deteriorate positioning accuracy, e.g. in a pick-and-place robot application.

Future work will include analysis of the disturbance rejection capabilities of the MALTA and an enhanced disturbance rejection position controller design. Additionally, stability limits with large radial and axial displacements of the mover will be studied.

APPENDIX

MALTA Parameters

The parameters of the MALTA prototype, used in the dynamic model, are given in **Tab. IV**. The analyzed operation of

the MALTA considers linear region where the force constants do not change with the amplitude of the phase currents.

TABLE IV: Mechanical Parameters of the MALTA.

Symbol	Quantity	Value
Mass and Moment of Inertia		
m	Mover Mass	0.360 kg
I_{xx}	Mover x -Axis MoI	$1.3805 \times 10^{-3} \text{ kg m}^2$
I_{yy}	Mover y -Axis MoI	$1.3805 \times 10^{-3} \text{ kg m}^2$
I_{zz}	Mover z -Axis MoI	$4.7707 \times 10^{-5} \text{ kg m}^2$
Force Constant		
K_D	Drive Const. per Module	5.2 N A^{-1}
K_B	Bearing Const. per Module	5.2 N A^{-1}
K_A	Attraction Const. per Module	8330 N m^{-1}

REFERENCES

- [1] B. Kou, J. Luo, X. Yang, and L. Zhang, "Modeling and Analysis of a Novel Transverse-Flux Flux-Reversal Linear Motor for Long-Stroke Application," *IEEE Trans. Ind. Electron.*, vol. 63, no. 10, pp. 6238–6248, 2016.
- [2] X. Zhen Huang, J. Li, Q. Tan, Z. Y. Qian, C. Zhang, and L. Li, "Sectional Combinations of the Modular Tubular Permanent Magnet Linear Motor and the Optimization Design," *IEEE Trans. Ind. Electron.*, 2018.
- [3] K. J. Meessen, J. J. Paulides, and E. A. Lomonova, "Modeling and Experimental Verification of a Tubular Actuator for 20g Acceleration in a Pick-and-Place Application," *IEEE Trans. Ind. Appl.*, vol. 46, no. 5, pp. 1891–1898, 2010.
- [4] T. Overboom, J. Jansen, E. Lomonova, and F. Tacke, "Design and Optimization of a Rotary Actuator for a Two-Degree-of-Freedom $z - \varphi$ Module," *IEEE Trans. Ind. Appl.*, vol. 46, no. 6, pp. 2401–2409, 2010.
- [5] T. J. Teo, H. Zhu, S.-L. Chen, G. Yang, and C. K. Pang, "Principle and Modelling of a Novel Moving Coil Linear-Rotary Electromagnetic Actuator," *IEEE Trans. Ind. Electron.*, vol. 63, no. 11, pp. 6930–6940, 2016.
- [6] P. R. Eckert, A. F. Flores Filho, E. Perondi, and D. G. Dorrell, "Dual Quasi-Halbach Linear Tubular Actuator with Coreless Moving-Coil for Semi-Active and Active Suspension," *IEEE Trans. Ind. Electron.*, 2018.
- [7] X. Xue, K. W. E. E. Cheng, and Z. Zhang, "Model, Analysis and Application of Tubular Linear Switched Reluctance Actuator for Linear Compressors," *IEEE Trans. Ind. Electron.*, 2018.
- [8] V. DelliColli, P. Cancelliere, F. Marignetti, R. DiStefano, and M. Sciarano, "A Tubular-Generator Drive for Wave Energy Conversion," *IEEE Trans. Ind. Electron.*, vol. 53, no. 4, pp. 1152–1159, 2006.
- [9] C.-T. Liu, C.-C. Hwang, and Y.-W. Chiu, "Design of a Coaxially Magnetic-Gear Linear Actuator for Electric Power Steering System Applications," *IEEE Trans. Ind. Appl.*, vol. 53, no. 3, pp. 2401–2408, 2017.
- [10] I. A. Smadi, H. Omori, and Y. Fujimoto, "Development, Analysis, and Experimental Realization of a Direct-Drive Helical Motor," *IEEE Transactions on Industrial Electronics*, vol. 59, no. 5, pp. 2208–2216, 2011.
- [11] S. Mirić, P. Küttel, A. Tüysüz, and J. W. Kolar, "Design and Experimental Analysis of a New Magnetically Levitated Tubular Linear Actuator," *IEEE Trans. Ind. Electron., Early Access*, 2018.
- [12] H. Bleuler, M. Cole, P. Keogh, R. Larssonneur, E. Maslen, Y. Okada, G. Schweitzer, A. Traxler *et al.*, *Magnetic Bearings: Theory, Design, and Application to Rotating Machinery*. Springer Science & Business Media, 2009.
- [13] S. Mirić, D. Bortis, and J. W. Kolar, "Design and Comparison of Permanent Magnet Self-Bearing Linear-Rotary Actuators," in *Proc. of 12th IEEE International Symposium on Linear Drives for Industry Applications (LDIA)*, 2019, pp. 1–6.
- [14] S.-L. Chen, T. Teo, and G. Yang, "Control of a Novel Linear-Rotary Actuator for High-Speed Pick-and-Place Application," *Australian Journal of Electric. and Electron. Eng.*, vol. 11, no. 3, pp. 289–296, 2014.
- [15] R. H. Bishop, *Mechatronic Systems, Sensors, and Actuators: Fundamentals and Modeling*. CRC Press Boca Raton, FL, ISBN 0-8493-9258-6, 2008.
- [16] J. Awrejcewicz and Z. Koruba, *Classical Mechanics: Applied Mechanics and Mechatronics*. Springer Science & Business Media, 2012, vol. 30.
- [17] P. Jin, H. Lin, S. Fang, and S. Ho, "Decoupling Control of Linear and Rotary Permanent Magnet Actuator Using Two-Directional $d - q$ Transformation," *IEEE Trans. on Magnetics*, vol. 48, no. 10, pp. 2585–2591, 2012.

- [18] S. Mirić, R. Giuffrida, D. Bortis, and J. W. Kolar, "Enhanced Complex Space Vector Modeling and Control System Design of Multiphase Magnetically Levitated Rotary-Linear Machines," *IEEE Journal of Emerging and Selected Topics in Power Electronics*, 2019.
- [19] L. Guzzella, *Analysis and Synthesis of Single-Input Single-Output Control Systems*. vdf Hochschulverlag AG, 2011.
- [20] K. J. Astrom and R. M. Murray, *Feedback Systems: An Introduction for Scientists and Engineers*. Princeton, NJ, USA: Princeton University Press, 2008.
- [21] S. Pan, P. A. Commins, and H. Du, "Tubular Linear Motor Position Detection by Hall-Effect Sensors," in *Proc. of IEEE Australasian Universities Power Engineering Conference (AUPEC)*, 2015, pp. 1–5.
- [22] A. Muesing, C. Zingerli, P. Imoberdorf, and J. W. Kolar, "PEEC-Based Numerical Optimization of Compact Radial Position Sensors for Active Magnetic Bearings," in *Proc. of VDE 5th International Conference on Integrated Power Electronics Systems*, 2008, pp. 1–5.
- [23] C. M. Zingerli, P. Imoberdorf, J. W. Kolar, and T. Nussbaumer, "Rotor Position Measurement for a Magnetically Levitated 500'000 rpm Permanent Magnet Machine," in *Proc. of IEEE Energy Conversion Congress and Exposition (ECCE USA)*, 2011, pp. 1778–1784.



Spasoje Mirić (S'13) received the B.Sc. and M.Sc. degrees in electrical engineering in 2012 and 2013, respectively, from the University of Belgrade, Belgrade, Serbia. He is currently working towards his Ph.D. degree in electrical engineering at the Swiss Federal Institute of Technology (ETH) Zurich, Zurich, Switzerland. His research interests are novel electrical machine topologies, linear machines and bearingless motors for highly dynamic actuator systems.



Rosario V. Giuffrida (S'19) received the B.Sc. degree in electronics engineering in 2016 from the University of Catania, Italy and the M.Sc. degree in Robotics, Systems and Control in 2019 from the Swiss Federal Institute of Technology (ETH) Zurich, Switzerland. Currently, he is with the Power Electronic Systems Laboratory at ETH Zurich for his Ph.D. studies. His research interests focus on design, sensing and motion control concepts for novel magnetically levitated actuators.



Dominik Bortis (M'08) received the M.Sc. and Ph.D. degree in electrical engineering from the Swiss Federal Institute of Technology (ETH) Zurich, Switzerland, in 2005 and 2008, respectively. In May 2005, he joined the Power Electronic Systems Laboratory (PES), ETH Zurich, as a Ph.D. student. From 2008 to 2011, he has been a Postdoctoral Fellow and from 2011 to 2016 a Research Associate with PES, co-supervising Ph.D. students and leading industry research projects. Since January 2016 Dr. Bortis

is heading the research group Advanced Mechatronic Systems at PES, which concentrates on ultra-high speed motors, magnetic bearings and bearingless drives, new linear-rotary actuator and machine concepts with integrated power electronics. In this context, multi-objective optimizations concerning weight/volume/efficiency/costs, the analysis of interactions of power electronics and electric machines, and EMI are given special attention. Targeted applications include advanced industry automation and manufacturing, e.g. highly dynamic and precise positioning systems, medical and pharmaceutical systems, e.g. ultra-high purity and blood pumps, and future mobility concepts, including motors and actuators for hybrid and electric vehicles, more electric aircraft and satellites. Dr. Bortis has published more than 90 scientific papers in international journals and conference proceedings. He has filed 32 patents and has received 6 IEEE Conference Prize Paper Awards.



Johann W. Kolar (F'10) is a Fellow of the IEEE and received his M.Sc. and Ph.D. degree (summa cum laude/promotio sub auspiciis praesidentis rei publicae) from the Vienna University of Technology, Austria, in 1997 and 1999, respectively. Since 1984, he has been working as independent researcher and international consultant in close collaboration with the Vienna University of Technology, in the fields of power electronics, industrial electronics and high performance drive systems. He is currently a Full

Professor and the Head of the Power Electronic Systems Laboratory at the Swiss Federal Institute of Technology (ETH) Zurich. He has proposed numerous novel PWM converter topologies, modulation and control concepts, multi-objective power electronics design procedures, etc. and has supervised 70+ Ph.D. students. He has published 900+ scientific papers in international journals and conference proceedings, 4 book chapters, and has filed 190+ patents. He has presented 30+ educational seminars at leading international conferences, has served as IEEE PELS Distinguished Lecturer from 2012 through 2016, and has received 34 IEEE Transactions and Conference Prize Paper Awards, the 2014 IEEE Power Electronics Society R. David Middlebrook Achievement Award, the 2016 IEEE William E. Newell Power Electronics Award, the 2016 IEEE PEMC Council Award, and two ETH Zurich Golden Owl Awards for excellence in teaching. He has initiated and/or is the founder of 4 ETH Spin-off companies. The focus of his current research is on ultra-compact and ultra-efficient SiC and GaN converter systems, ANN-based power electronics components and systems design, Solid-State Transformers, Power Supplies on Chip, as well as ultra-high speed and ultra-light weight drives, bearingless motors, and energy harvesting.